Monolithic all-perovskite tandem solar cells with 24.8% efficiency exploiting comproportionation to suppress Sn(II) oxidation in precursor ink

Renxing Lin[1,5], Ke Xiao[1,5], Zhengyuan Qin[2], Qiaolei Han[1], Chunfeng Zhang [2]*, Mingyang Wei [3], Makhsud I. Saidaminov [3], Yuan Gao[1], Jun Xu[4], Min Xiao[1,2], Aidong Li[1], Jia Zhu [1]*, Edward H. Sargent [3] and Hairen Tan [1]*

Combining wide-bandgap and narrow-bandgap perovskites to construct monolithic all-perovskite tandem solar cells offers avenues for continued increases in photovoltaic (PV) power conversion efficiencies (PCEs). However, actual efficiencies today are diminished by the subpar performance of narrow-bandgap subcells. Here we report a strategy to reduce Sn vacancies in mixed Pb–Sn narrow-bandgap perovskites that use metallic tin to reduce the Sn^{4+} (an oxidation product of Sn^{2+}) to Sn^{2+} via a comproportionation reaction. We increase, thereby, the charge-carrier diffusion length in narrow-bandgap perovskites to 3 μm for the best materials. We obtain a PCE of 21.1% for 1.22-eV narrow-bandgap solar cells. We fabricate monolithic all-perovskite tandem cells with certified PCEs of 24.8% for small-area devices (0.049 cm^2) and of 22.1% for large-area devices (1.05 cm^2). The tandem cells retain 90% of their performance following 463 h of operation at the maximum power point under full 1-sun illumination.

O wing to long carrier diffusion lengths, low trap densities and high tolerance to defects, lead halide perovskite solar cells (PSCs) have recently seen rapid advances in power conversion efficiency (PCE), reaching certified efficiencies of 24.2% (refs. [1–3]). Combining Pb-based wide-bandgap perovskites (~1.8 eV) with mixed Pb–Sn-based narrow-bandgap perovskites (~1.2 eV) to construct monolithic tandem solar cells offers the potential to achieve even higher PCEs than single-junction PSCs[4–6].

Alloying Pb and Sn in metal halide perovskites provides a route to obtain narrow bandgaps (E_g) down to 1.17 eV for Sn content of 50–60% (refs. [7–9]). However, a key element in these perovskites, Sn^{2+}, is prone to oxidation, forming Sn^{4+}, especially in precursor solutions and SnI$_2$ solids, leading to high trap densities and short diffusion lengths in tin-containing perovskites[10–12]. To address this limitation, tin source purification and antioxidant additives such as SnF$_2$, SnF$_2$-pyrazine complex and hydroxybenzene sulfonic acid have been used to reduce defect densities related to Sn^{2+} oxidation in Sn-halide perovskites[13–17]. Device engineering strategies such as engineering the interface[18–20], enlarging grains[21,22], introducing lattice strain[23] and alloying using halides[22,24] have been exploited in mixed Pb–Sn narrow-bandgap PSCs to achieve improved PCEs of 17–19%. Guanidinium thiocyanate was recently reported to passivate grain boundaries and reduce surface defect densities; this increased the carrier lifetime and thus the diffusion length of mixed Pb–Sn perovskites, and led to PCEs of 20.2% (with a short-circuit current density J_{sc} of ~30 mA cm^{-2}) for single-junction narrow-bandgap PSCs and 23.1% (area ~0.1 cm^2) for monolithic all-perovskite tandem solar cells[25]. We reasoned that reducing the in-grain defect density (that is, Sn vacancies) would enable us to improve the PCE further.

The efficiency of all-perovskite tandem solar cells remains below its potential due to the low external quantum efficiencies (EQEs) in the near-infrared range[22,25–28], and lags behind the single-junction Pb-based PSCs. It is particularly noticeable for commercially relevant large-area (≥1 cm^2) devices: a highest PCE of 13.3% was reported for all-perovskite tandems whereas Pb-based single-junction PSCs have demonstrated certified PCEs of 20.9% (refs. [3,27]). Long-term device operational stability of all-perovskite tandems has also remained far inferior to that of Pb-based single-junction devices[22,25–27,29].

The tunnel recombination junction in monolithic all-perovskite tandems typically relies on a sputtered indium tin oxide (ITO) layer to protect the underlying layers during solution processing of the back narrow-bandgap subcells[22,25,26,30]. The thick ITO layer not only induces parasitic absorption loss in the near-infrared spectral range, but it also causes shunting between subcells that severely constrains the performance of large-area devices and prevents the cell-to-cell monolithic integration in thin-film modules[31]. Recently, Palmstrom et al. showed that the thick ITO layer can be avoided by forming a dense recombination layer via atomic layer deposition, resulting in improved performance in all-perovskite tandem solar cells[32].

Here we report a simple and effective tin-reduced precursor (TRP) solution strategy that prevents the oxidation of Sn^{2+} to Sn^{4+} in the precursor solution of narrow-bandgap perovskites by adding a small amount of metallic tin powders; the leftover tin granules are removed before film fabrication via filtering solution. By using this strategy, we are able to reduce the Sn vacancies inside the grains and thereby achieve a long carrier diffusion length of 3 μm in mixed Pb–Sn perovskite films, with electronic quality comparable to high-quality full Pb-based perovskites that have a diffusion

[1]National Laboratory of Solid State Microstructures, Jiangsu Key Laboratory of Artificial Functional Materials, College of Engineering and Applied Sciences, Nanjing University, Nanjing, China. [2]School of Physics, Nanjing University, Nanjing, China. [3]Department of Electrical and Computer Engineering, University of Toronto, Toronto, Ontario, Canada. [4]School of Electronics Science and Engineering, Nanjing University, Nanjing, China. [5]These authors contributed equally: Renxing Lin, Ke Xiao. *e-mail: cfzhang@nju.edu.cn; jiazhu@nju.edu.cn; hairentan@nju.edu.cn

length of 3.5 μm and PCEs higher than 22%. We obtained the highest PCE of 21.1% for 1.22-eV mixed Pb–Sn narrow-bandgap PSCs, together with a fill factor (FF) above 80% and J_{sc} values higher than 32 mA cm^{-2}. We further developed a recombination junction that avoids using sputtered ITO by taking the advantage of a robust and compact SnO$_2$ layer processed with atomic layer deposition. These enabled us to fabricate monolithic all-perovskite tandem solar cells with certified PCEs of 24.8% for a small-area device (0.049 cm^2) and 22.1% for a large-area device (1.05 cm^2) under reverse scans. The tandem solar cells exhibited promising stability, retaining 90% of their initial performance following 463 h of operation at the maximum power point (MPP) under full 1-sun illumination.

Low-E_g perovskites thin films via comproportionation

The performance and operational stability of mixed Pb–Sn narrow-bandgap PSCs suffers from a high defect density (that is, Sn vacancies) in the bulk and surfaces of mixed Pb–Sn perovskites due to the ready oxidation of Sn^{2+} to Sn^{4+}. This occurs especially in the precursor solutions and in SnI$_2$ solids[10,33,34]. It leads to short charge-carrier lifetimes and thus short diffusion lengths in tin-containing perovskite films, resulting in poor charge transport/extraction and low FF values in solar cells.

We observed that as-prepared yellow perovskite precursor solution, which contained a mixture of SnI$_2$, PbI$_2$, SnF$_2$, formamidinium iodide (FAI) and methylammonium iodide (MAI) in mixed dimethylformamide (DMF) and dimethylsulfoxide (DMSO) solvents, became orange-red rapidly following exposure to air (Fig. 1a and Supplementary Fig. 1). This indicates that Sn^{2+} readily oxidizes to Sn^{4+} in the precursor solution, and that the commonly used reducing agent additive SnF$_2$ does not prevent completely the oxidation of Sn^{2+}, and does not sufficiently reduce Sn^{4+} to Sn^{2+} once Sn^{4+} forms in the precursor solution.

We posited that the trap density in mixed Pb–Sn perovskites could be reduced if the undesired Sn^{4+}—already formed in perovskite precursor solution—could be avoided in the precursor solution before film formation. In contrast with purely Sn-based perovskites, mixed Pb–Sn perovskites (in their solid film form) with SnF$_2$ embedded in the grains are tolerant to Sn^{2+} oxidation even in ambient air[26,27,35], and the oxidation of Sn^{2+} to Sn^{4+} is expected to occur mainly before film formation in mixed Pb–Sn perovskite systems.

We pursued a reducing agent that is insoluble in precursor solution on its own, but becomes a part of the perovskite lattice once oxidized by Sn^{4+} to form Sn^{2+}. We constructed the Frost diagram for Sn of different oxidation states (Supplementary Fig. 2) and found that metallic Sn readily reduces Sn^{4+} in the precursor solution via the comproportionation reaction Sn+Sn^{4+} → 2Sn^{2+}; the standard redox potential of this reaction is $E^o = 0.29$ V, exhibiting negative Gibbs energy $\Delta G^o = -nFE^o < 0$ (ref. [36]), where n is the electron transfer number and F is the Faraday constant. Indeed, when we added metallic Sn powders into oxidized Pb–Sn perovskite precursor solution, the red solution became bright yellow again, even in the presence of oxygen, indicating that Sn^{4+} had been reduced to Sn^{2+} in the presence of metallic Sn (Supplementary Fig. 1).

The transmittance spectra of the precursor solution further confirmed the colour changes at different stages (Supplementary Fig. 2). We found that the absorption edge of the pristine precursor solution blue-shifted slightly following the introduction of Sn powders, a finding we attribute to the reduction of Sn^{4+} formed already in the solution (even in the glovebox) in the absence of Sn powders. In comparison, the precursor solution with Sn powders maintained its bright-yellow colour even after exposure to air for at least 2 weeks. We believed that the formation of Sn vacancies due to the presence of Sn^{4+} in the precursor solution could potentially be suppressed in perovskite films processed from Sn^{4+}-free precursor solution (Fig. 1b).

We fabricated mixed Pb–Sn narrow-bandgap perovskite films with a composition of MA$_{0.3}$FA$_{0.7}$Pb$_{0.5}$Sn$_{0.5}$I$_3$ from pristine (referred to as control from hereon) and TRP solutions using the antisolvent method. The metallic Sn powders (microparticles with a diameter of ~150 μm) were completely removed via filtering through a 0.2-μm polytetrafluoroethylene (PTFE) membrane filter; no metallic Sn was detected via X-ray photoemission spectroscopy (XPS; Supplementary Fig. 3) in the TRP perovskite films. The TRP perovskite films showed a substantially reduced concentration of Sn^{4+} compared to control films (Supplementary Fig. 3a–c). The Sn^{4+} in control films is assigned principally to the precursor solids (SnI$_2$) and further oxidation of Sn^{2+} to Sn^{4+} in the precursor solution. We found that even highest-purity (99.999%) SnI$_2$ beads available from Alfa Aesar and Sigma-Aldrich exhibited a substantial amount of Sn^{4+} (Supplementary Fig. 3d). We noted also that the SnI$_2$ beads, marked as the same purity (99.999%), exhibited different colours for materials provided by Alfa Aesar and Sigma-Aldrich (Supplementary Fig. 4), and the colour of beads varied from batch to batch from the same provider.

The narrow-bandgap perovskite films showed an optical bandgap (defined at absorption onset) of 1.22 eV (Supplementary Fig. 5). The control and TRP perovskite films exhibited a pure perovskite phase with similar crystallinity and crystallographic orientation (Fig. 1c). Both films exhibited photoluminescence peaks at 1,000 nm, but the TRP perovskite film showed stronger photoluminescence intensity due to reduced non-radiative recombination (Fig. 1d). Both control and TRP films are smooth and pinhole-free, with uniform and large grains (Fig. 1e,f). Cross-sectional scanning electron microscopy (SEM) images (Supplementary Fig. 6) indicated that mixed Pb–Sn narrow-bandgap perovskite films form vertically oriented grains, offering potential benefits to charge transport in solar cells.

Charge transport characteristics of low-E_g perovskites

To measure the charge transport characteristics, we carried out femtosecond- and nanosecond-resolved optical-pump terahertz-probe (OPTP) spectroscopy, a non-destructive method of probing the photoinduced conductivity and charge-carrier mobility[37,38]. Transient THz spectroscopy (1 THz ≈ 4.1 meV) is suitable for the sensing of photocarriers and their dynamics, since THz spectroscopy is sensitive to the free charge carriers but not to the bound carriers such as excitons and trapped carriers. Fluence-dependent femtosecond OPTP transients exhibited accelerated decay dynamics at higher initial photoinjected charge-carrier densities due to the enhanced contributions from bimolecular and Auger recombination (Fig. 2a,b). We calculated recombination rate constants and charge-carrier mobilities of 72 and 79 cm^2 V^{-1} s^{-1} for control and TRP samples, respectively. The derivation of mobility and other parameters from OPTP transients is detailed in Methods and Supplementary Note 1.

We then performed nanosecond OPTP spectroscopy and extracted charge-carrier lifetimes of 3 ns versus 43 ns for control and TRP perovskite films (Fig. 2c). The much longer lifetime in TRP film agrees with the picture of a significantly lowered trap density. We derived the charge-carrier diffusion lengths (L_D) as a function of the charge-carrier density n following the equation[37]: $L_D = [\mu k_B T/(qR)]^{1/2}$, where $R = k_1+nk_2+n^2k_3$ is the total recombination rate, k_B is the Boltzmann constant, T is the absolute temperature and q is the elementary charge. Under 1-sun solar illumination conditions ($n \approx 10^{15}$ cm^{-3})[38], the diffusion lengths of control and TRP perovskite films are 0.75 and 2.99 μm, respectively. The diffusion length of TRP narrow-bandgap perovskites is therefore several times longer than the thickness (~1 μm) required for complete incident light absorption in solar cells, and this fact ensures efficient carrier extraction in thick solar cells as required for efficient light harvesting in tandem devices. The TRP mixed Pb–Sn perovskites show a diffusion length comparable to those in high-quality Pb-based 1.53-eV perovskites
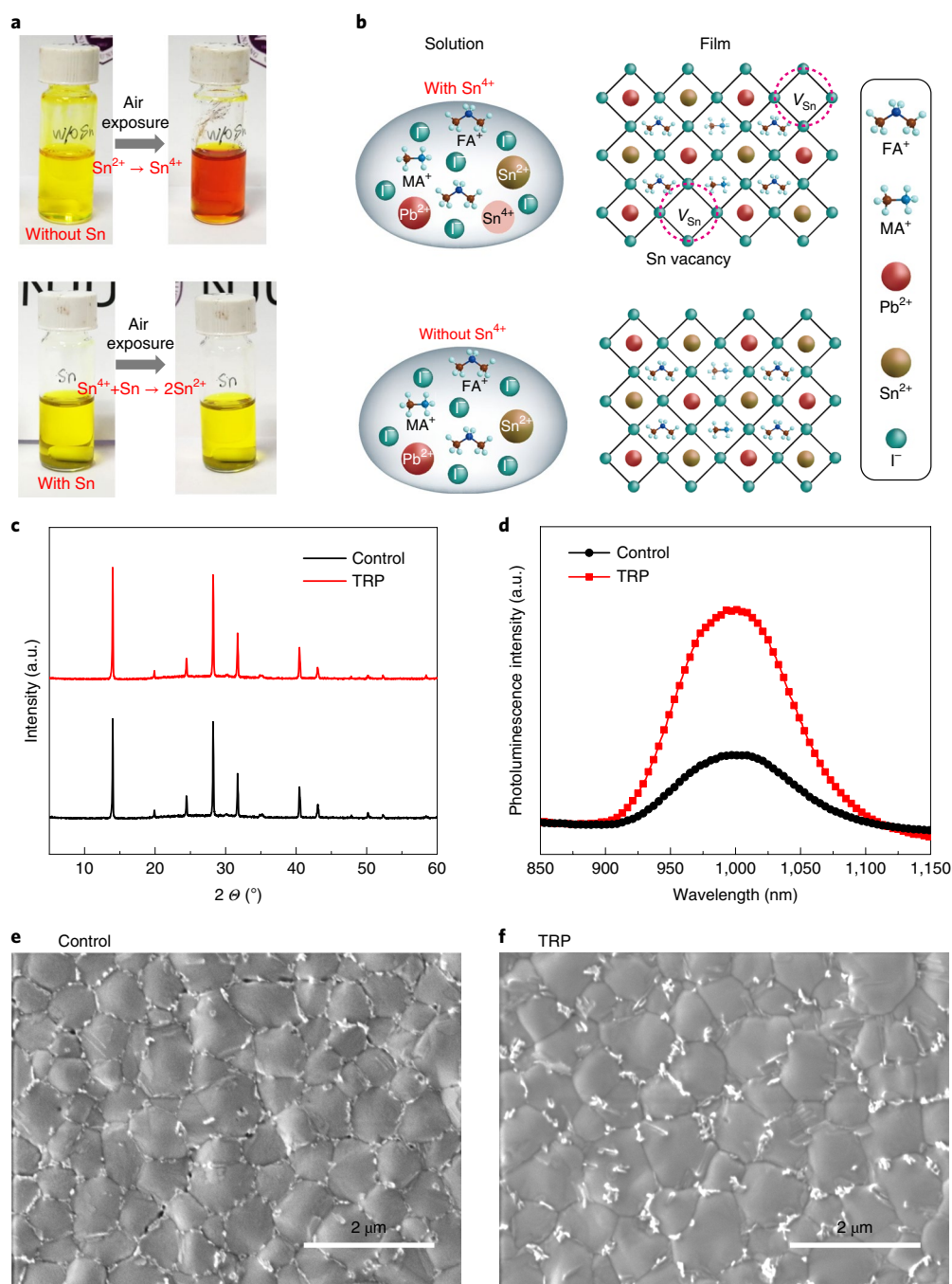
Fig. 1 | Mixed Pb–Sn narrow-bandgap perovskite films fabricated from Sn⁴⁺-containing and Sn-reduced (Sn⁴⁺-free) precursor solutions. a, Photographs showing the ease of oxidation of Sn^{2+} to Sn^{4+} in ambient air and the facile reduction of Sn^{4+} to Sn^{2+} by metallic Sn powders. **b**, Illustration of the formation of Sn vacancies in mixed Pb–Sn perovskite due to the presence of Sn^{4+} in the precursor solution and the suppression of Sn vacancy formation in TRP perovskite because of the absence of Sn^{4+}. **c**, X-ray diffraction patterns of control and TRP narrow-bandgap perovskite films. a.u., arbitrary units. **d**, Photoluminescence spectra of control and TRP narrow-bandgap perovskites films deposited on bare glass substrates. **e,f**, SEM images of control (**e**) and TRP (**f**) narrow-bandgap perovskite films.

($L_D = 3.45\,\mu m$) with a composition of $Cs_{0.05}MA_{0.05}FA_{0.9}PbI_{2.85}Br_{0.15}$ that delivers PCEs higher than 22% (Supplementary Figs. 7–9).

To explore the origins of improved charge-carrier lifetimes and diffusion lengths in TRP narrow-bandgap perovskites, we carried out space-charge-limited current and Mott–Schottky plot measurements to estimate the trap density and hole concentration for control and TRP films (Supplementary Figs. 10 and 11). As expected, mixed Pb–Sn perovskites exhibit a high hole concentration, and the density of hole traps is higher than the density of electron traps due to the tendency to form Sn vacancies in the material (Table 1). By avoiding Sn^{4+} in the precursor solution, the density of hole traps is reduced from $2.14 \times 10^{16}\,cm^{-3}$ for the control samples to $1.06 \times 10^{16}\,cm^{-3}$ for the TRP films. Correspondingly, the hole concentration is significantly decreased from $1.4 \times 10^{16}\,cm^{-3}$ in the control samples made from Sn^{4+}-containing solution to $0.54 \times 10^{16}\,cm^{-3}$ in the TRP ones.
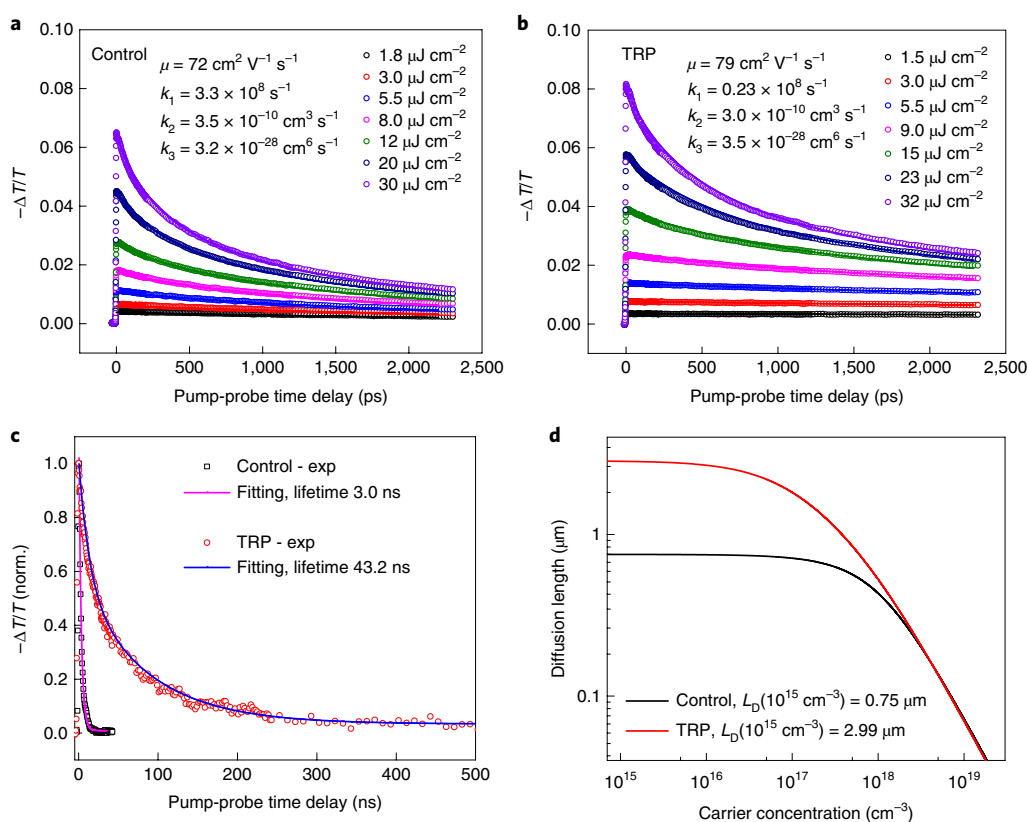
Fig. 2 | Charge dynamics of mixed Pb–Sn narrow-bandgap perovskites. a,b, Femtosecond OPTP transients for control (**a**) and TRP (**b**) perovskite films measured after excitation with a 90-fs light pulse of 800 nm wavelength with various fluences. The rate constants (k) associated with different recombination processes were fitted globally to these transients according to the equation $dn(t)/dt = -k_3 n^3 - k_2 n^2 - k_1 n$, where t is decay time, and k_1, k_2, k_3 are rate constants associated with monomolecular recombination, bimolecular recombination and Auger recombination, respectively. The mobilities are calculated to 72 and 79 cm² V⁻¹ s⁻¹ for the control and TRP samples, respectively. **c**, Nanosecond OPTP transients for the control and TRP perovskite films measured after excitation with a 0.8-ns light pulse of 800 nm wavelength with a low fluence. The lifetimes were obtained by the monoexponential fit. All OPTP measurements were carried out in a N_2 atmosphere to avoid potential degradation of samples in ambient air. norm., normalized; exp, experimental data. **d**, Charge-carrier diffusion lengths (L_D) of control and TRP perovskite films as a function of charge-carrier concentration. At 1-sun condition (a carrier density of approximately 10^{15} cm⁻³), the control and TRP samples show diffusion lengths of 0.75 and 2.99 μm, respectively.

Table 1 | Material characteristics of mixed Pb–Sn perovskites and full Pb-based perovskite

Material	Composition	$N_{trap,\,electron}$	$N_{trap,\,hole}$	N_{hole}	Mobility	Lifetime	L_D
		(10^{16} cm⁻³)	(10^{16} cm⁻³)	(10^{16} cm⁻³)	(cm² V⁻¹ s⁻¹)	(ns)	(μm)
Pb–Sn, control	$MA_{0.3}FA_{0.7}Pb_{0.5}Sn_{0.5}I_3$	0.38	2.14	1.40	72	3	0.75
Pb–Sn, TRP	$MA_{0.3}FA_{0.7}Pb_{0.5}Sn_{0.5}I_3$	0.24	1.06	0.54	79	43	2.99
Full Pb, 1.53 eV	$Cs_{0.05}MA_{0.05}FA_{0.9}Pb(I_{0.95}Br_{0.05})_3$	0.13	0.38	–	55	82	3.45

$N_{trap,\,electron}$, density of electron traps; $N_{trap,\,hole}$, density of hole traps; N_{hole}, hole density.

PV performance of low-E_g PSCs

We fabricated a series of mixed Pb–Sn narrow-bandgap PSCs with various absorber layer thicknesses to evaluate solar cell performance (Fig. 3a and Supplementary Table 1). The devices had an inverted planar structure comprising ITO/PEDOT:PSS/mixed Pb–Sn perovskite/C₆₀/BCP/Cu (Supplementary Fig. 6), where PEDOT:PSS is poly(3,4-ethylene dioxythiophene)-poly(styrene sulfonate), C₆₀ is fullerene and BCP is bathocuproine. For very thin devices, that is, at a thickness of 220 nm, both control and TRP devices were not limited by their diffusion lengths and they exhibited comparable performance. As the thickness of perovskite absorber increased from 350 to 920 nm, the TRP devices exhibited considerably better performance than the control devices. The

average FF value of TRP devices was substantially constant for all thicknesses investigated, and the average J_{sc} value gradually increased with thickness due to increased light absorption when the thicker absorber was used, and this was achieved without compromising the carrier collection, as indicated by the EQE curves in Fig. 3b. By contrast, the average FF value of control devices decreased with thickness, consistent with the shorter diffusion length. Correspondingly, the control devices initially showed increased J_{sc} with thickness up to 650 nm, up to which the charge transport was not severely constrained by the diffusion length. As the thickness increased beyond their diffusion length, that is, at 860 and 920 nm thickness, the control devices exhibited reduced J_{sc} with increased thickness and photogenerated charge carriers were
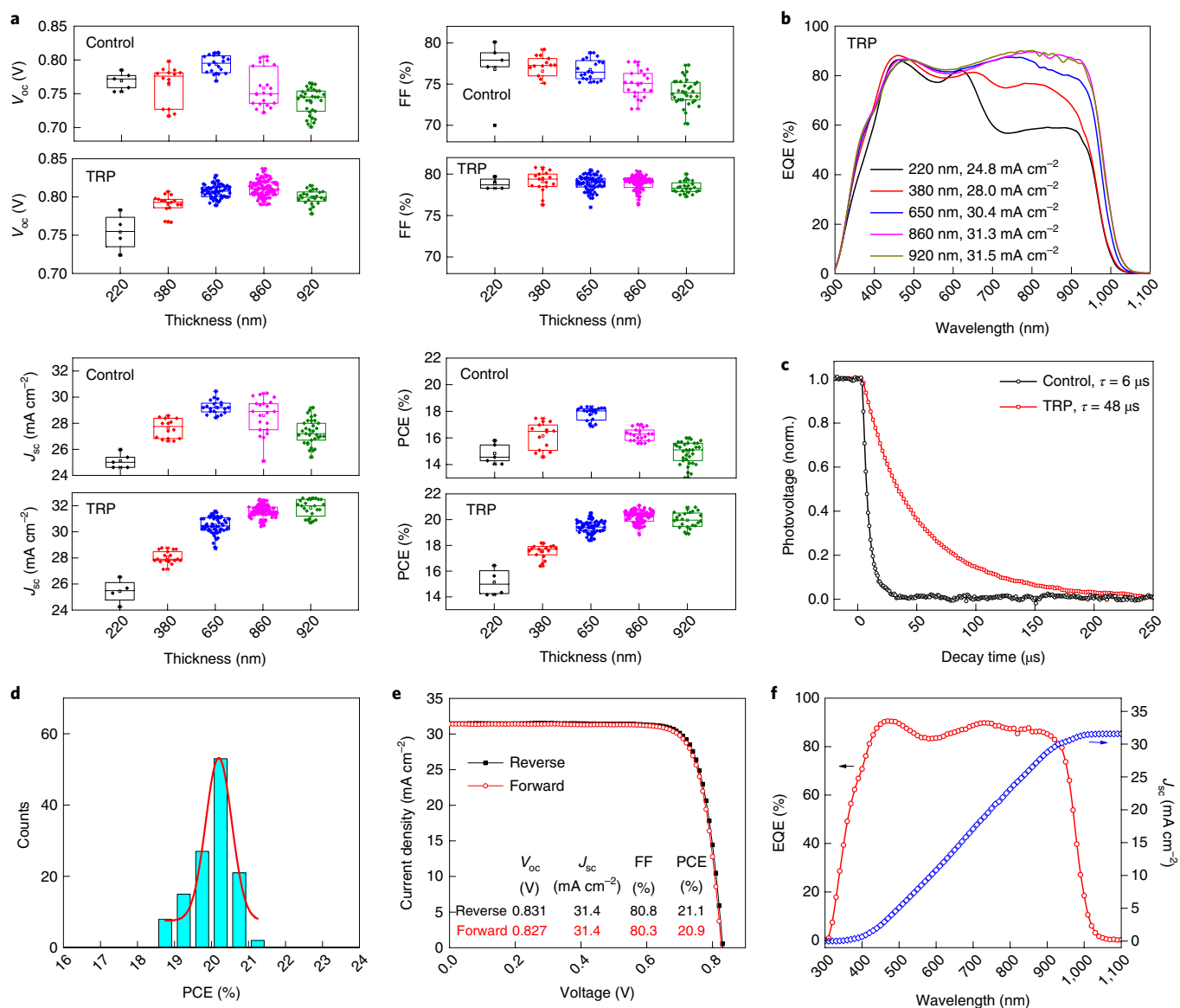
Fig. 3 | PV performance of mixed Pb–Sn narrow-bandgap PSCs. a, PV parameters of control and TRP solar cells with various perovskite layer thicknesses. **b**, Representative EQE curves of TRP solar cells with various perovskite thicknesses. **c**, Transient photovoltage decay of control and TRP solar cells with a thickness of 860 nm. The recombination lifetime (τ) is monoexponentially fitted. **d**, Histogram of PCEs over 126 TRP devices with a perovskite layer thickness of 860 nm. The devices exhibit an average PCE of 20.1 ± 0.6%. **e**, J–V curves of the best-performing TRP device. **f**, EQE curve of the best-performing TRP device, showing an integrated J_{sc} of 31.6 mA cm^{-2}.

not efficiently extracted, as indicated by the EQE curves shown in Supplementary Fig. 12.

The best performance for control devices was achieved at a thickness of 650 nm, with an average PCE of 17.8% and a best PCE of 18.3% (V_{oc} = 0.811 V, FF = 77.7%, J_{sc} = 29.1 mA cm^{-2} where V_{oc} is open-circuit voltage; Supplementary Fig. 13), which is comparable to previously reported performance[22–24]. The TRP devices obtained their best performance using an 860-nm-thick absorber, resulting in a considerably higher average PCE of 20.1%. Further increasing the thickness beyond this thickness did not lead to an obvious increase in J_{sc} due to almost complete light absorption. The devices with thick absorbers reached highest J_{sc} values above 32 mA cm^{-2}, which is amongst the highest values reported[24–26,32]. It is interesting to note that the average V_{oc} of TRP solar cells increases with thickness up to 860 nm. This can be ascribed to the larger grain size formed at a higher concentration of precursor solution (Supplementary Fig. 14) and is consistent with previous studies[21,26]. The best V_{oc} (0.84 V)

achieved in our devices is still below the best reported values (0.85–0.89 V)[19,22,24]. Further optimization of perovskite composition, device interface and grain passivation offers the potential to achieve higher V_{oc} and FF values[19,20,24,25,28]. We performed transient photovoltage decay under the open-circuit condition for control and TRP solar cells (Fig. 3c) and found that the charge-recombination lifetime τ of the TRP device (48 µs) was substantially longer than that of the control device (6 µs), consistent with the longer charge-carrier lifetime and lower trap density in TRP perovskite films (Fig. 2 and Table 1). The TRP solar cells also exhibited lower dark saturation-current density (Supplementary Fig. 15), in agreement with lower trap density and lower hole concentration in TRP perovskite films[24].

Figure 3d shows a histogram of PCE values over 126 TRP narrow-bandgap PSCs at the optimal thickness of 860 nm. The devices have an average PCE of 20.1 ± 0.6%, and the narrow PCE distribution indicates an excellent reproducibility for devices processed from the TRP solution. The best TRP narrow-bandgap PSC achieved a high
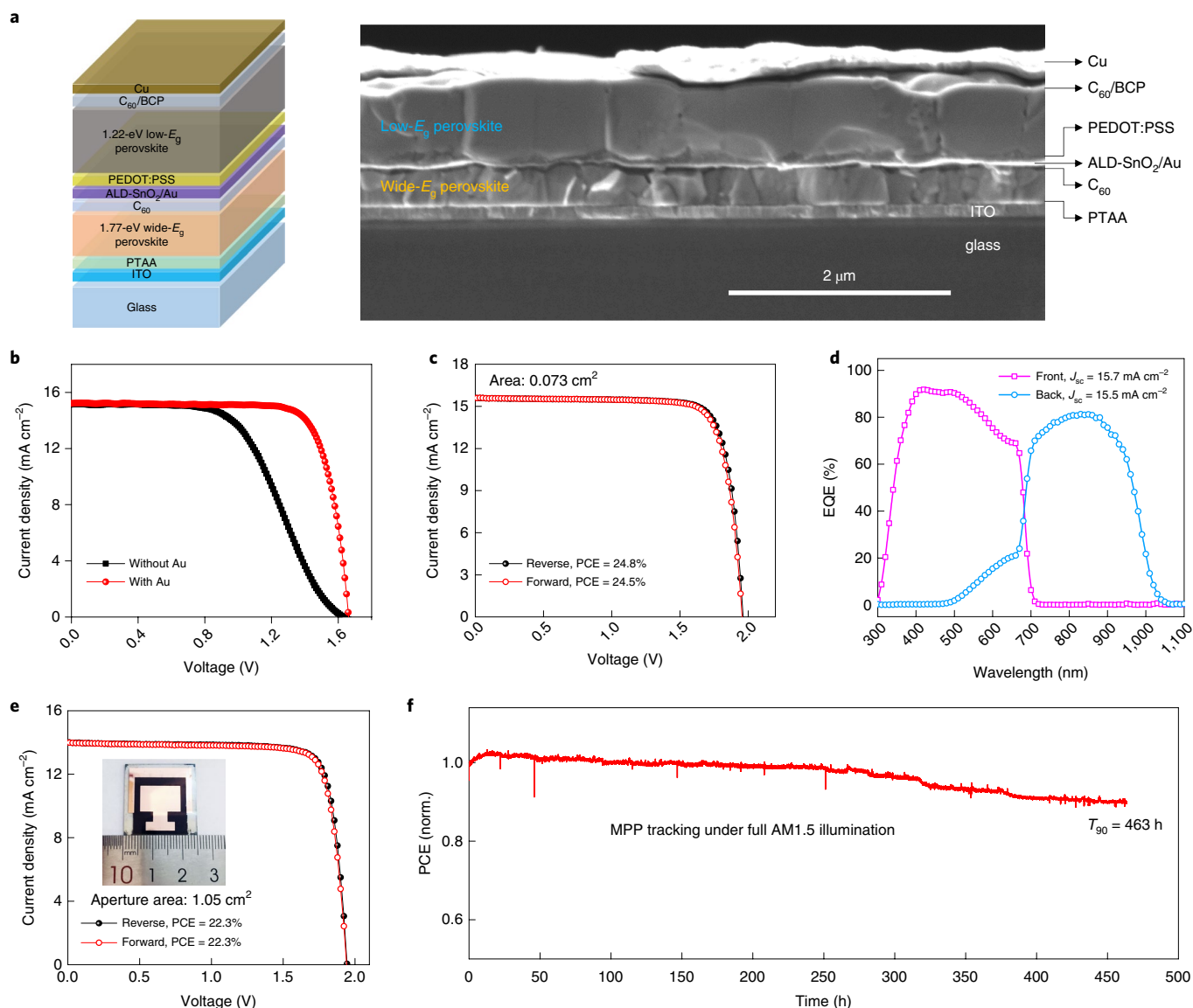
Fig. 4 | Performance and stability of monolithic all-perovskite tandem solar cells. a, Device structure and corresponding cross-sectional SEM image of a tandem solar cell. **b**, J–V curves of tandem solar cells without and with an ultrathin Au layer in the tunnel recombination junction. **c**, J–V curves of the best-performing small-area tandem solar cell (0.073 cm²), showing PCEs of 24.8% and 24.5% under reverse and forward scans, respectively. **d**, EQE curves of the best-performing small-area tandem cell, showing integrated J_{sc} values of 15.7 and 15.5 mA cm⁻² for the front and back subcells, respectively. **e**, J–V curves of a large-area tandem solar cell (1.05 cm²). The inset shows the digital photo of the large-area device. **f**, MPP tracking of an unencapsulated small-area tandem solar cell for 463 h in a glovebox under full simulated AM1.5 solar illumination (100 mW cm⁻²) without ultraviolet filter. The device retained 90% of its initial efficiency after operation for 463 h (T_{90} = 463 h). AM1.5, Air Mass 1.5.

PCE of 21.1% under reverse scan and a PCE of 20.9% under forward scan, showing low hysteresis (Fig. 3e). The stabilized power output of 20.9% is consistent with the PCEs determined from the current density–voltage (J–V) sweeps (Supplementary Fig. 16). The integrated J_{sc} value from the EQE curve is 31.6 mA cm⁻², which is in good agreement with the values obtained from J–V measurements (Fig. 3f). The devices show a spectral response up to 1,050 nm wavelength and exhibit high EQE values in the near-infrared spectral range (above 80% for wavelengths up to 940 nm). We sent a narrow-bandgap solar cell to an accredited independent PV test laboratory (SIMIT, Shanghai, China) for certification (see Methods about the PV certification at Shanghai Institute of Microsystem and Information Technology (SIMIT)), and the device delivered a certified PCE of 19.83% (Supplementary Fig. 17). Another device was sent to Newport PV test laboratory (Montana, USA), and the device

delivered a comparable certified PCE of 19.53% (Supplementary Fig. 18). Minor drops in PCE (~5% relatively) were observed after exposure to ambient air during shipping to and testing at SIMIT and Newport.

Performance and stability of all-perovskite tandems

We fabricated monolithic all-perovskite tandem cells using a 1.77-eV wide-bandgap front subcell (~300 nm) and a 1.22-eV TRP narrow-bandgap back subcell (~800 nm) as depicted in Fig. 4a. The wide-bandgap perovskite had composition $Cs_{0.2}FA_{0.8}PbI_{1.8}Br_{1.2}$. The tandem cells had a device configuration of glass/ITO/PTAA/wide-E_g perovskite/C_{60}/ALD-SnO₂/Au(~1 nm)/ PEDOT:PSS/low-E_g perovskite/C_{60}/BCP/Cu, where PTAA is poly(triarylamine). Here we took advantage of depositing a compact thin layer of SnO₂ using atomic layer deposition (ALD) to avoid the necessity of ITO layer in

Table 2 | PV performance of monolithic tandem solar cells and single-junction subcells

Cells	Scan direction	V_{oc} (V)	J_{sc} (mA cm^{-2})	FF (%)	PCE (%)
1.77-eV single	Reverse	1.216	17.0	79.7	16.5
	Forward	1.202	17.0	79.9	16.3
2T tandem (0.073 cm^2)	Reverse	1.965	15.6	81.0	24.8
	Forward	1.957	15.6	80.2	24.5
2T tandem (1.05 cm^2)	Reverse	1.945	14.0	82.0	22.3
	Forward	1.943	14.0	81.8	22.3

Reverse, scan from V_{oc} to J_{sc}; forward, scan from J_{sc} to V_{oc}; 2T, two-terminal.

the tunnel recombination junction. The ALD-SnO$_2$ layer provides excellent electron extraction and leads to slightly improved performance for the wide-bandgap front cells (Supplementary Fig. 19). This compact and robust ALD-SnO$_2$ layer (~20 nm thick) allowed us to fabricate tandems free of ITO layer, as the SnO$_2$ layer can prevent damage to the deposited-underlying front subcells during the solution processing of back subcells. An ultrathin Au layer (~1 nm) was deposited between the SnO$_2$ and PEDOT:PSS layers by thermal evaporation to facilitate electron–hole recombination in the tunnel recombination junction. Tandem solar cells without the ultrathin Au layer exhibited an obvious S shape in the J–V curves near the open-circuit voltage and thus have low FF values (Fig. 4b and Supplementary Table 2).

Figure 4c,d presents the J–V and EQE curves of the best-performing tandem solar cells; the corresponding PV parameters are summarized in Table 2. The champion tandem device exhibits a high PCE of 24.8% under reverse scan, with a high V_{oc} of 1.965 V, a J_{sc} of 15.6 mA cm^{-2} and a high FF of 81.0%. The V_{oc} of tandem cells closely approaches the summed photovoltages of the two subcells, indicating negligible voltage loss in the interconnecting recombination junction. The PCE of tandem cells reported herein are appreciably higher than that of each subcell, indicating the benefits of the monolithic tandem configuration. The tandem devices and corresponding single-junction subcells exhibit low hysteresis between reverse and forward scans (Table 2). The PCEs from J–V sweeps are consistent with the stabilized PCE of 24.5% in tandem devices (Supplementary Fig. 20). These PCEs are high when compared to other monolithic all-perovskite tandem solar cell reports. The integrated J_{sc} values of the front and back subcells from EQE curves (Fig. 4d) are 15.7 and 15.5 mA cm^{-2}, respectively, agreeing well with the J_{sc} determined from J–V measurements. Supplementary Table 3 shows the summary of performance over 26 tandem solar cells processed among several batches. The tandem devices provide an average PCE of 22.6 ± 0.9%, best V_{oc} values exceeding 2.0 V and a relatively narrow PCE distribution indicative of promising reproducibility.

To evaluate the upscaling potential of tandem cells, we also fabricated large-area devices (1.05 cm^2 aperture area) with processing and perovskite absorbers as used in small cells. The large-area cells exhibited a high PCE of 22.3% (V_{oc} =1.945 V, J_{sc} = 14.0 mA cm^{-2} and FF = 82.0%) without detailed optimization for current matching between subcells (Fig. 4e). The J_{sc} value is lower than that of the small-area cell due to the use of a thicker front ITO electrode—this leads to stronger parasitic absorption in the near-infrared spectral range and thus lower photocurrent in the back subcell (Supplementary Fig. 21). The V_{oc} and FF values of large-area devices are comparable to those seen in small-area devices (Table 2). The performance of these large-area tandems indicates promise in upscaling all-perovskite tandem solar cells. We sent a small-area

(aperture area 0.049 cm^2) and a large-area (1.05 cm^2) tandem solar cell to SIMIT (Shanghai, China) for certification, and the devices delivered certified PCEs of 24.8% and 22.1% under reverse scans, respectively (Supplementary Figs. 22 and 23).

Stability is another crucial parameter for commercialization of PSCs. We anticipated that reducing the lattice defects, that is, the Sn vacancies, in the TRP narrow-bandgap perovskites would allow us to improve the stability of tandem solar cells[39,40]. We first investigated the shelf lifetime of tandem solar cells, storing the devices in a glovebox in the dark and tracking the evolution of PCEs. Supplementary Fig. 24 shows that there is no obvious degradation in performance following dark storage in a nitrogen atmosphere for 1,650 h. This indicates that the stability of mixed Pb–Sn perovskites is achievable using suitable encapsulation.

We also investigated the operational stability of unencapsulated tandem cells under full 1-sun illumination and MPP operation in a glovebox without ultraviolet filter. The PCE of tandem cells increased slightly in the first tens of hours of illumination, which may be related to light-induced defect healing in perovskites[41,42]. The tandem solar cells exhibited promising stability for Sn-containing PSCs and retained 90% of their initial performance following operation for 463 h under 1-sun illumination with MPP tracking (Fig. 4f).

Conclusions

In summary, we have developed a strategy to reduce Sn vacancies in mixed Pb–Sn narrow-bandgap perovskites via a comproportionation reaction, and increased thereby the performance and stability of monolithic all-perovskite tandem solar cells. We obtained a PCE of 21.1% (certified 19.5%) for mixed Pb–Sn single-junction solar cells, and achieved certified PCEs of 24.8% and 22.1% for small-area and large-area all-perovskite tandem solar cells, respectively. The tandem cells exhibit promising stability and retain 90% of their performance after 463 h of operation at the MPP under full 1-sun illumination. Efficiency of the monolithic all-perovskite tandem solar cells is still limited by the large V_{oc} deficit in the wide-bandgap front cell and the optical loss caused by the tunnel recombination junction. The sum of the EQEs in the tandem solar cell is considerably lower than that of single-junction narrow-bandgap solar cells over 680–1,000 nm wavelength range due to optical reflection and parasitic absorption by the PEDOT:PSS layer in the recombination junction (Supplementary Fig. 25). Further advances in wide-bandgap PSCs and tunnel recombination junctions should enable PCEs exceeding 25%, making all-perovskite tandem PV technologies promising, in view of the potential for low cost combined with higher efficiencies.

Methods

Materials. Unless otherwise stated, all materials were purchased from Sigma-Aldrich or Alfa Aesar and used as received without further purification. Unless otherwise stated, all films and devices discussed herein were fabricated using SnI$_2$ (99.999% purity) purchased from Alfa Aesar without further purification. The organic halide salts were purchased from GreatCell Solar (Australia). PEDOT:PSS aqueous solution (Al 4083) was purchased from Heraeus Clevios (Germany). Tin powders were purchased from Sigma-Aldrich (<150 μm, 99.5%).

Perovskite precursor solution. To make narrow-bandgap FA$_{0.7}$MA$_{0.3}$Pb$_{0.5}$Sn$_{0.5}$I$_3$ perovskite films with various thicknesses, the precursor solution (with various concentrations of 0.8, 1.2, 1.6, 1.8 and 2.0 M) was prepared in mixed solvents of DMF and DMSO with a volume ratio of 3:1. The molar ratios for FAI/MAI and PbI$_2$/SnI$_2$ were 0.7:0.3 and 0.5:0.5, respectively. The molar ratio of (FAI+MAI)/(PbI$_2$+SnI$_2$) was 1:1. SnF$_2$ (10 mol% relative to SnI$_2$) was added in the precursor solution. The precursor solution was stirred at room temperature for 2 h and then filtered through 0.20-μm PTFE membrane before use. To reduce Sn^{4+} in the precursor solution, tin powders (5 mg ml^{-1}) were added in the precursor and stirred at room temperature for 10 min before use. The precursor solution with the remaining tin powders was filtered through 0.20-μm PTFE membrane before the perovskite films were made. XPS measurements did not detect any residual metallic Sn in the perovskite films. It should be noted that SnF$_2$ additive is still necessary in TRP solution to achieve high performance in solar cells (see Supplementary Figs. 26 and 27). To make wide-bandgap FA$_{0.8}$Cs$_{0.2}$Pb(I$_{0.6}$Br$_{0.4}$)$_3$ perovskite films, the precursor solution (1.1 M) was prepared in mixed solvents of DMF and

DMSO with a volume ratio of 4:1. The molar ratios for FAI/FABr/CsI/CsBr and $PbI_2/PbBr_2$ were 0.48:0.32:0.12:0.08 and 0.6:0.4, respectively. The molar ratio of $(FAI+FABr+CsI+CsBr)/(PbI_2+PbBr_2)$ was 1:1. The precursor solution was stirred at 50 °C for 2 h and then filtered through a 0.20-μm PTFE membrane before use.

Pb–Sn narrow-bandgap PSC fabrication. The pre-patterned ITO glass substrates were sequentially cleaned using acetone and isopropanol. PEDOT:PSS (Al 4083) was spin-coated on ITO substrates at 4,000 r.p.m. for 30 s and annealed on a hotplate at 150 °C for 10 min in ambient air. After cooling, we transferred the substrates immediately to a nitrogen-filled glovebox for the deposition of perovskite films. The perovskite films were deposited with two-step spin-coating procedures: (1) 1,000 r.p.m. for 10 s with an acceleration of 200 r.p.m. s^{-1} and (2) 4,000 r.p.m. for 40 s with a ramp-up of 1,000 r.p.m. s^{-1}. Ethyl acetate (200 μl) was dropped on the spinning substrate during the second spin-coating step at 20 s before the end of the procedure. Ethyl acetate was chosen here since it is less toxic and more environmentally friendly than commonly used chlorobenzene. The substrates were then transferred to a hotplate and heated at 100 °C for 10 min. After cooling down to room temperature, the substrates were transferred to the evaporation system. Finally, C_{60}(20 nm)/BCP(7 nm)/Cu(100 nm) were sequentially deposited on top of the perovskite by thermal evaporation.

Monolithic all-perovskite tandem solar cell fabrication. PTAA (2 mg mL^{-1} in chlorobenzene) layers were firstly spin-coated on ITO substrates at 5,000 r.p.m. for 30 s and annealed on a hotplate at 150 °C for 10 min in a glovebox. After cooling, the wide-bandgap perovskite films were deposited on top of PTAA with a two-step spin-coating procedure. The first step was 2,000 r.p.m. for 10 s with an acceleration of 200 r.p.m. s^{-1}. The second step was 6,000 r.p.m. for 40 s with a ramp-up of 2,000 r.p.m. s^{-1}. Chlorobenzene (100 μl) was dropped onto the spinning substrate during the second spin-coating step at 20 s before the end of the procedure. The substrates were then transferred on a hotplate and heated at 100 °C for 15 min. After cooling down to room temperature, the substrates were transferred to the evaporation system, and 20-nm-thick C_{60} film was subsequently deposited on top by thermal evaporation at a rate of 0.2 Å s^{-1}. The substrates were then exposed to air and transferred to the ALD system to deposit a 20-nm SnO_2 layer at low temperatures. After ALD deposition, the substrates were exposed to air again and transferred to the thermal evaporation system to deposit an ultrathin layer of Au clusters (~1 nm) on SnO_2. PEDOT:PSS layers were spin-cast on top of the SnO_2-protected front cell and annealed in air at 120 °C for 20 min. After the substrates had cooled, we immediately transferred the substrates to a nitrogen-filled glovebox for the deposition of narrow-bandgap perovskite films with identical procedures used for the single-junction devices. We found that the thickness of the Pb–Sn narrow-bandgap perovskite film was slightly thinner than that of the film in the single-junction device even though we used identical process and precursor solution. Finally, 20-nm C_{60}, 7-nm BCP and 100-nm Cu films were sequentially deposited by thermal evaporation at the rates of 0.2, 0.2 and 1.0 Å s^{-1}, respectively.

Characterization of single-junction narrow-bandgap solar cells. The J–V characteristics were measured using a Keithley 2400 sourcemeter under the illumination of the solar simulator (EnliTech, Class AAA) at a light intensity of 100 mW cm^{-2} as checked with a calibrated reference solar cell (NREL) with a quartz window (a KG-5 reference cell was used for the measurements of the wide-bandgap solar cell). Unless otherwise stated, the J–V curves were all measured in a nitrogen-filled glovebox with a scanning rate of 100 mV s^{-1} (with a voltage step of 10 mV and a delay time of 100 ms). The steady-state PCE, PCE(t), was measured by setting the bias voltage to the V_{MPP} and then tracing the current density, where the V_{MPP} at MPP was determined from the J–V curve. The active area was determined by the aperture shade mask (0.073 cm^2) placed in front of the solar cell to avoid overestimation of the photocurrent density. An aperture mask with a smaller open area (0.049 cm^2) was used for the measurements at Newport or SIMIT to avoid misalignment between the cell and the mask; however, this underestimated the measured open-circuit voltages. EQE measurements were performed in ambient air without encapsulation using a QE system (EnliTech) with monochromatic light focused on the device pixel and a chopper frequency of 20 Hz. The reference cell used for the calibration of EQE measurements was calibrated by NREL.

Characterization of tandem solar cells. The J–V characteristics were measured with a dual-lamp (xenon and halogen) class AAA solar simulator (Yamashita Denso, YSS-T155-2M). The two lamps (xenon and halogen) were finely tuned to ensure that spectra mismatch was within 3% over 400–500, 500–600, 600–700, 700–800 and 800–900 nm wavelength ranges (Supplementary Fig. 28). The solar simulator was set at a light intensity of 100 mW cm^{-2} as checked with a calibrated crystalline silicon reference solar cell with a quartz window. EQE measurements were performed in ambient air with bias voltages of 1.1 and 0.7 V for front and back subcells, respectively. We noticed that there was no obvious difference for the EQE measurements with or without bias voltages. The bias illumination from highly-bright light-emitting diodes (LEDs) with emission peaks of 850 and 460 nm were used for the measurements of the front subcells and back subcells,

respectively. The operational stability tests were carried out under full AM1.5G illumination (xenon lamp solar simulator, 100 mW cm^{-2}) in a glovebox by fixing the voltage at V_{MPP} and then tracking the current output. The solar cells were not encapsulated and no ultraviolet filter was applied. The solar cell temperature increased to ~32 °C during the long-time MPP tests as no passive cooling was implemented. The illumination intensity was regularly calibrated to compensate for the gradual degradation of the xenon lamp. The dark long-term stability assessments of solar cells (without encapsulation) were carried out by repeating the J–V characterizations over various times and the devices were stored in a N_2 glovebox.

Femtosecond and nanosecond OPTP spectroscopy. For femtosecond OPTP spectroscopy, a commercial titanium–sapphire amplified laser (Libra, Coherent) with a pulse duration of 90 fs, centre wavelength of 800 nm and repetition rate of 1 kHz was used to generate THz radiation via optical rectification in a 0.5-mm-thick ZnTe(110) nonlinear single crystal and detect it using free space electro-optic sampling in a 0.5-mm-thick ZnTe(110) crystal. Perovskite thin films deposited on z-cut quartz substrates were photoexcited at 800 nm with fluences in the range 1.5–50 μJ cm^{-2}. The change in THz amplitude was monitored as a function of the time delay between the 800-nm optical-pump pulse and THz probe pulse using a translation stage. For nanosecond OPTP spectroscopy, we used a frequency-doubled subnanosecond laser (Picolo AOT MOPA, InnoLas) with a pulse duration of ~0.8 ns to excite the samples at 532 nm. The laser was synchronized to the THz probe pulse with an electronic delay generator (SRS DG645, Stanford Research System). All measurements were carried out in a nitrogen-purged environment to avoid potential degradation of perovskite films in ambient air.

As the excitation fluence increased, the OPTP transients exhibited accelerated decay dynamics at higher initial photoinjected charge-carrier densities due to enhanced contributions from bimolecular recombination and Auger recombination. We extracted the rate constants associated with different recombination mechanisms by global fits to these transients according to the following rate equation[37]:

$$\frac{dn(t)}{dt} = -k_3 n^3 - k_2 n^2 - k_1 n$$

The femtosecond OPTP transients did not exhibit obvious decay dynamics at low excitation density, which makes it difficult to extract an accurate rate constant k_1. To extract k_1 as well as charge-carrier lifetime, we then performed nanosecond OPTP spectroscopy by changing the photoexcitation source while keeping the sample inside the measurement chamber. The samples were photoexcited at a low fluence to reduce the effects of bimolecular and Auger recombination. The nanosecond OPTP transients were fitted with a monoexponential decay function. A carrier density of 10^{15} cm^{-3} (1-sun condition) was used as being representative of typical operating conditions for a solar cell.

Space-charge-limited current. The hole-only or electron-only devices were fabricated to obtain the density of hole traps or electron traps using the following architectures: ITO/PEDOT:PSS/perovskite/PTAA/Au for holes, where the PTAA layer was doped with 5 wt% 4-isopropyl-4'-methyldiphenyliodoniumtetrakis (pentafluorophenyl)borate[43], and ITO/TiO$_2$-Cl/PCBM/perovskite/C_{60}/BCP/Cu for electrons, where PCBM is [6,6]-phenyl C_{61} butyric acid methyl ester. Measurements were carried out in a glovebox using a Keithley 2400 sourcemeter. The applied voltages started from 0 V and rose to 5 V with an interval of 0.01 V and a delay time of 100 ms. The trap density N_{trap} is determined by the equation $V_{TFL} = qN_{trap}L^2/(2\varepsilon\varepsilon_0)$, where V_{TFL} is thte trap-filled limit voltage, L is the thickness of perovskite film, ε is the relative dielectric constant of perovskite (32 for all samples) and ε_0 is the vacuum permittivity.

Other characterizations. SEM images were obtained using a TESCAN microscope with an accelerating voltage of 2 kV. X-ray diffraction patterns were collected using a Rigaku MiniFlex 600 diffractometer equipped with a NaI scintillation counter and using monochromatized Cu Kα radiation (wavelength λ = 1.5406 Å). XPS analysis was carried out using a Thermo Scientific Al K-Alpha XPS system with energy steps of 0.1 eV. Optical absorption measurements were carried out in a Lambda 950 ultraviolet/visible spectrophotometer (Perkin Elmer). Photoluminescence was measured using a FLS980 fluorescence spectrometer (Edinburgh Instruments) equipped with time-correlated single-photon-counting system. The light was illuminated from the perovskite film side and the excitation wavelength was 405 nm. Transient photovoltage decays were measured on a home-made system. A 540-nm green LED was used to modulate the V_{oc} with a constant light bias and the repetition rate was set to 2,000 Hz. A white LED was focused on the active area of the solar cell under study for the constant light bias. The intensity of the pulsed illumination was set in a way that the modulated V_{oc} was ~10 mV to ensure a perturbation regime. The open-circuit voltage transient, induced by the light perturbation, was measured with a digital oscilloscope set to an input impedance of 1 MΩ. The charge-recombination lifetime was fitted by a single exponential decay. The Mott–Schottky plot measurements were performed on a CHI660 electrochemical workstation (CH Instrument Inc.) at a frequency of 1 kHz from −0.8 to 0.8 V with a voltage step of 10 mV.

PV certification at SIMIT (Shanghai, China). The PV certification tests were performed by the Test and Calibration Centre of the New Energy Device and Module, SIMIT, Chinese Academy of Sciences, which is accredited by China National Accreditation Service for Conformity Assessment (CNAS) to ISO/IEC 17025 and by the International Laboratory Accreditation Cooperation (ILAC) Mutual Recognition Arrangement. CNAS was the accreditation body member of the International Accreditation Forum and ILAC, and is also a member of the Asia Pacific Laboratory Accreditation Cooperation and Pacific Accreditation Cooperation.

The J-V characteristics were measured using a steady-state class AAA dual-lamp (xenon and halogen) super solar simulator under standard test conditions according to IEC 60904-1:2006. The J–V curves were measured in forward and reverse scans with a scanning speed of $50\,mV\,s^{-1}$. A World PV Scale (WPVS) silicon reference solar cell calibrated by NREL was used to set the irradiance at $100\,mW\,cm^{-2}$. The spectral mismatch was calculated and mismatch correction was performed according to IEC 60904-7:2008. The spectral irradiance of the solar simulator was measured by a calibrated spectroradiometer (Opto Research Corporation), and the EQE of the device under test was measured with a three-grating monochromator spectral response measurement system.

The measurements of tandem solar cells were performed according to IEC 60904-1-1 for J–V measurements and to IEC 60904-8-1 for EQE measurements. The full-spectral mismatch factor of the solar simulator for our tandem solar cells was 1.00 ± 0.01, representing an excellent spectrum matching with AM1.5G.

Reporting summary. Further information on research design is available in the Nature Research Reporting Summary linked to this article.

Data availability
All data that support the findings in this study are present in the paper and the Supplementary Information. Additional data related to this study are available from the corresponding authors upon reasonable request.

References

1. Rong, Y. et al. Challenges for commercializing perovskite solar cells. *Science* **361**, eaat8235 (2018).
2. Jiang, Q. et al. Surface passivation of perovskite film for efficient solar cells. *Nat. Photonics* **13**, 460–466 (2019).
3. Green, M. A. et al. Solar cell efficiency tables (version 54). *Prog. Photovolt. Res. Appl.* **27**, 565–575 (2019).
4. Eperon, G. E., Hörantner, M. T. & Snaith, H. J. Metal halide perovskite tandem and multiple-junction photovoltaics. *Nat. Rev. Chem.* **1**, 0095 (2017).
5. Leijtens, T., Bush, K. A., Prasanna, R. & McGehee, M. D. Opportunities and challenges for tandem solar cells using metal halide perovskite semiconductors. *Nat. Energy* **3**, 828–838 (2018).
6. Wang, C., Song, Z., Li, C., Zhao, D. & Yan, Y. Low-bandgap mixed tin-lead perovskites and their applications in all-perovskite tandem solar cells. *Adv. Funct. Mater.* 1808801 (2019).
7. Hao, F., Stoumpos, C. C., Chang, R. P. H. & Kanatzidis, M. G. Anomalous band gap behavior in mixed Sn and Pb perovskites enables broadening of absorption spectrum in solar cells. *J. Am. Chem. Soc.* **136**, 8094–8099 (2014).
8. Ogomi, Y. et al. $CH_3NH_3Sn_xPb_{(1-x)}I_3$ perovskite solar cells covering up to 1060 nm. *J. Phys. Chem. Lett.* **5**, 1004–1011 (2014).
9. Liao, W. et al. Fabrication of efficient low-bandgap perovskite solar cells by combining formamidinium tin iodide with methylammonium lead iodide. *J. Am. Chem. Soc.* **138**, 12360–12363 (2016).
10. Konstantakou, M. & Stergiopoulos, T. A critical review on tin halide perovskite solar cells. *J. Mater. Chem. A* **5**, 11518–11549 (2017).
11. Ke, W. & Kanatzidis, M. G. Prospects for low-toxicity lead-free perovskite solar cells. *Nat. Commun.* **10**, 965 (2019).
12. Chung, I. et al. $CsSnI_3$: semiconductor or metal? High electrical conductivity and strong near-infrared photoluminescence from a single material. High hole mobility and phase-transitions. *J. Am. Chem. Soc.* **134**, 8579–8587 (2012).
13. Ma, L. et al. Carrier diffusion lengths of over 500 nm in lead-free perovskite $CH_3NH_3SnI_3$ films. *J. Am. Chem. Soc.* **138**, 14750–14755 (2016).
14. Liao, W. et al. Lead-free inverted planar formamidinium tin triiodide perovskite solar cells achieving power conversion efficiencies up to 6.22%. *Adv. Mater.* **28**, 9333–9340 (2016).
15. Lee, S. J. et al. Fabrication of efficient formamidinium tin iodide perovskite solar cells through SnF_2–pyrazine complex. *J. Am. Chem. Soc.* **138**, 3974–3977 (2016).
16. Tai, Q. et al. Antioxidant grain passivation for air-stable tin-based perovskite solar cells. *Angew. Chem. Int. Ed.* **58**, 806–810 (2019).
17. Gu, F. et al. Improving performance of lead-free formamidinium tin triiodide perovskite solar cells by tin source purification. *Sol. RRL* **2**, 1800136 (2018).
18. Rajagopal, A., Liang, P.-W., Chueh, C.-C., Yang, Z. & Jen, A. K. Y. Defect passivation via a graded fullerene heterojunction in low-bandgap Pb–Sn binary perovskite photovoltaics. *ACS Energy Lett.* **2**, 2531–2539 (2017).
19. Xu, G. et al. Integrating ultrathin bulk-heterojunction organic semiconductor intermediary for high-performance low-bandgap perovskite solar cells with low energy loss. *Adv. Funct. Mater.* **28**, 1804427 (2018).
20. Tang, H., Shang, Y., Zhou, W., Peng, Z. & Ning, Z. Energy level tuning of PEDOT:PSS for high performance tin-lead mixed perovskite solar cells. *Sol. RRL* **3**, 1800256 (2019).
21. Zhao, D. et al. Low-bandgap mixed tin–lead iodide perovskite absorbers with long carrier lifetimes for all-perovskite tandem solar cells. *Nat. Energy* **2**, 17018 (2017).
22. Zhao, D. et al. Efficient two-terminal all-perovskite tandem solar cells enabled by high-quality low-bandgap absorber layers. *Nat. Energy* **3**, 1093–1100 (2018).
23. Prasanna, R. et al. Band gap tuning via lattice contraction and octahedral tilting in perovskite materials for photovoltaics. *J. Am. Chem. Soc.* **139**, 11117–11124 (2017).
24. Li, C. et al. Reducing saturation-current density to realize high-efficiency low-bandgap mixed tin-lead halide perovskite solar cells. *Adv. Energy Mater.* **9**, 1803135 (2019).
25. Tong, J. et al. Carrier lifetimes of >1 µs in Sn-Pb perovskites enable efficient all-perovskite tandem solar cells. *Science* **364**, 475–479 (2019).
26. Leijtens, T. et al. Tin–lead halide perovskites with improved thermal and air stability for efficient all-perovskite tandem solar cells. *Sustain. Energy Fuels* **2**, 2450–2459 (2018).
27. Eperon, G. E. et al. Perovskite-perovskite tandem photovoltaics with optimized band gaps. *Science* **354**, 861–865 (2016).
28. Rajagopal, A. et al. Highly efficient perovskite-perovskite tandem solar cells reaching 80% of the theoretical limit in photovoltage. *Adv. Mater.* **29**, 1702140 (2017).
29. Jung, E. H. et al. Efficient, stable and scalable perovskite solar cells using poly(3-hexylthiophene). *Nature* **567**, 511–515 (2019).
30. Rajagopal, A., Stoddard, R. J., Jo, S. B., Hillhouse, H. W. & Jen, A. K. Overcoming the photovoltage plateau in large bandgap perovskite photovoltaics. *Nano Lett.* **18**, 3985–3993 (2018).
31. Sahli, F. et al. Improved optics in monolithic perovskite/silicon tandem solar cells with a nanocrystalline silicon recombination junction. *Adv. Energy Mater.* **8**, 1701609 (2018).
32. Palmstrom, A. F. et al. Enabling flexible all-perovskite tandem solar cells. *Joule* 1–12 https://doi.org/10.1016/j.joule.2019.05.009 (2019).
33. Lee, S. J. et al. Reducing carrier density in formamidinium tin perovskites and its beneficial effects on stability and efficiency of perovskite solar cells. *ACS Energy Lett.* **3**, 46–53 (2018).
34. Stoumpos, C. C., Malliakas, C. D. & Kanatzidis, M. G. Semiconducting tin and lead iodide perovskites with organic cations: phase transitions, high mobilities, and near-infrared photoluminescent properties. *Inorg. Chem.* **52**, 9019–9038 (2013).
35. Leijtens, T., Prasanna, R., Gold-Parker, A., Toney, M. F. & McGehee, M. D. Mechanism of tin oxidation and stabilization by lead substitution in tin halide perovskites. *ACS Energy Lett.* **2**, 2159–2165 (2017).
36. Vanýsek, P. *Handbook of Chemistry and Physics* 93rd edn (Ed. Haynes, W. M.) 5–80 (Chemical Rubber Company, 2012).
37. Wehrenfennig, C., Eperon, G. E., Johnston, M. B., Snaith, H. J. & Herz, L. M. High charge carrier mobilities and lifetimes in organolead trihalide perovskites. *Adv. Mater.* **26**, 1584–1589 (2014).
38. McMeekin, D. P. et al. A mixed-cation lead mixed-halide perovskite absorber for tandem solar cells. *Science* **351**, 151–155 (2016).
39. Saidaminov, M. I. et al. Suppression of atomic vacancies via incorporation of isovalent small ions to increase the stability of halide perovskite solar cells in ambient air. *Nat. Energy* **3**, 648–654 (2018).
40. Aristidou, N. et al. Fast oxygen diffusion and iodide defects mediate oxygen-induced degradation of perovskite solar cells. *Nat. Commun.* **8**, 15218 (2017).
41. Saliba, M. et al. Incorporation of rubidium cations into perovskite solar cells improves photovoltaic performance. *Science* **354**, 206–209 (2016).
42. Tan, H. et al. Efficient and stable solution-processed planar perovskite solar cells via contact passivation. *Science* **355**, 722–726 (2017).
43. Han, Q. et al. High-performance perovskite/$Cu(In,Ga)Se_2$ monolithic tandem solar cells. *Science* **361**, 904–908 (2018).

Acknowledgements

Author contributions

H.T. conceived the idea and directed the overall project. R.L., K.X., C.Z., J.Z., E.H.S. and H.T. designed the experiments. R.L. and K.X. fabricated all the devices and conducted the characterization. Z.Q., C.Z. and M.X. carried out the THz measurements and corresponding data analysis. Q.H., M.W., M.I.S. and Y.G. helped on the device fabrication and characterization. A.L. helped on ALD processing. J.X. helped on ultraviolet–visible–near-infrared spectroscopy measurements. H.T. and E.H.S. wrote the manuscript, and all authors read and commented on the manuscript.

Competing interests

The authors declare no competing interests.

Additional information

Supplementary information is available for this paper at https://doi.org/10.1038/s41560-019-0466-3.

Correspondence and requests for materials should be addressed to C.Z., J.Z. or H.T.

Reprints and permissions information is available at www.nature.com/reprints.

Publisher's note Springer Nature remains neutral with regard to jurisdictional claims in published maps and institutional affiliations.

nature research

Corresponding author(s):   Hairen Tan, Jia Zhu, Chunfeng Zhang

Solar Cells Reporting Summary

Nature Research wishes to improve the reproducibility of the work that we publish. This form is intended for publication with all accepted papers reporting the characterization of photovoltaic devices and provides structure for consistency and transparency in reporting. Some list items might not apply to an individual manuscript, but all fields must be completed for clarity.

For further information on Nature Research policies, including our data availability policy, see Authors & Referees.

▶ Experimental design

Please check: are the following details reported in the manuscript?

1. Dimensions

   Area of the tested solar cells
   ☒ Yes
   ☐ No
   The areas are 0.073 and 1.05 cm2 for small-area and large-area devices, respectively.

   Method used to determine the device area
   ☒ Yes
   ☐ No
   The areas are defined by the aperture areas of metallic masks.

2. Current-voltage characterization

   Current density-voltage (J-V) plots in both forward and backward direction
   ☒ Yes
   ☐ No
   Both forward and backward scans are provided to check the device hysteresis.

   Voltage scan conditions
   For instance: scan direction, speed, dwell times
   ☒ Yes
   ☐ No
   Explained in Methods.

   Test environment
   For instance: characterization temperature, in air or in glove box
   ☒ Yes
   ☐ No
   Explained in Methods.

   Protocol for preconditioning of the device before its characterization
   ☐ Yes
   ☒ No
   No preconditioning was implemented before characterization.

   Stability of the J-V characteristic
   Verified with time evolution of the maximum power point or with the photocurrent at maximum power point; see ref. 7 for details.
   ☒ Yes
   ☐ No
   Given in main text and supplementary information.

3. Hysteresis or any other unusual behaviour

   Description of the unusual behaviour observed during the characterization
   ☒ Yes
   ☐ No
   Low hysteresis was observed for some solar cells reported herein.

   Related experimental data
   ☒ Yes
   ☐ No
   Forward and backward J-V scans are provided in main text and supplementary information.

4. Efficiency

   External quantum efficiency (EQE) or incident photons to current efficiency (IPCE)
   ☒ Yes
   ☐ No
   Given in the main texts and supplementary information.

   A comparison between the integrated response under the standard reference spectrum and the response measure under the simulator
   ☒ Yes
   ☐ No
   The integrated Jsc values are consistent with those from J-V measurements.

   For tandem solar cells, the bias illumination and bias voltage used for each subcell
   ☒ Yes
   ☐ No
   Explained in Methods.

5. Calibration

   Light source and reference cell or sensor used for the characterization
   ☒ Yes
   ☐ No
   Explained in Methods.

   Confirmation that the reference cell was calibrated and certified
   ☒ Yes
   ☐ No
   The reference cell was calibrated by NREL and explained in Methods.

Calculation of spectral mismatch between the reference cell and the devices under test

☐ Yes
☒ No

> The light spectrum used for measurements matches well with the reference cell and AM1.5, and we used mismatched factor of 1 for all devices.

6. Mask/aperture

Size of the mask/aperture used during testing

☒ Yes
☐ No

> Metal aperture masks with areas of 0.073 and 1.05 cm2 were used for testing.

Variation of the measured short-circuit current density with the mask/aperture area

☐ Yes
☒ No

> We measured all devices with identical masks.

7. Performance certification

Identity of the independent certification laboratory that confirmed the photovoltaic performance

☒ Yes
☐ No

> The Pb-Sn single-junction solar cell was certified by Newport and SIMIT. The tandem devices were certified by SIMIT. Details about the certification center - SIMIT can be found in Methods.

A copy of any certificate(s)
Provide in Supplementary Information

☒ Yes
☐ No

> Given in the Supplementary Information.

8. Statistics

Number of solar cells tested

☒ Yes
☐ No

> More than 100 devices were tested for TRP Pb-Sn single junction solar cells. More than 20 devices were tested for tandem solar cells.

Statistical analysis of the device performance

☒ Yes
☐ No

> Given in the main text and supplementary information.

9. Long-term stability analysis

Type of analysis, bias conditions and environmental conditions
For instance: illumination type, temperature, atmosphere humidity, encapsulation method, preconditioning temperature

☒ Yes
☐ No

> Explained in Methods.